

SHORT TOPICS

10.1002/2014MS000322

Key Points:

- HPR is calculated on a global long-term scale with a large amount in the ITCZ
- HPR induces appreciable regional impact on TLSA simulation in northern winter
- HPR helps to reduce TLSA simulation biases by up to 1 K at continental scales

Supporting Information:

- Readme
- Figures S1–S2

Correspondence to:

Y. Dai,
yongjiudai@bnu.edu.cn

Citation:

Wei, N., Y. Dai, M. Zhang, L. Zhou, D. Ji, S. Zhu, and L. Wang (2014), Impact of precipitation-induced sensible heat on the simulation of land-surface air temperature, *J. Adv. Model. Earth Syst.*, 6, 1311–1320, doi:10.1002/2014MS000322.

Received 14 MAR 2014

Accepted 13 OCT 2014

Accepted article online 20 OCT 2014

Published online 5 DEC 2014

This is an open access article under the terms of the Creative Commons Attribution-NonCommercial-NoDerivs License, which permits use and distribution in any medium, provided the original work is properly cited, the use is non-commercial and no modifications or adaptations are made.

Impact of precipitation-induced sensible heat on the simulation of land-surface air temperature

Nan Wei¹, Yongjiu Dai¹, Minghua Zhang², Liming Zhou³, Duoying Ji¹, Siguang Zhu¹, and Lili Wang¹

¹College of Global Change and Earth System Science, Beijing Normal University, Beijing, China, ²School of Marine and Atmospheric Sciences, Stony Brook University, Stony Brook, New York, USA, ³Department of Atmospheric and Environmental Sciences, State University of New York at Albany, Albany, New York, USA

Abstract Precipitation-induced sensible heat (HPR) which is transferred between the land surface and rainwater can be extremely large during a heavy precipitation event. Thus, the local surface temperature can be sharply altered on an hourly to daily timescale. However, HPR is commonly neglected in current land surface models because of its small magnitude on long timescales. As a consequence, the simulated land-surface air temperature (TLSA) may be biased. In this study, we use satellite and reanalysis data sets to estimate HPR on the global scale, and we use CESM1 (with CAM4 physics and the prescribed sea surface temperature) to investigate the effect of HPR on TLSA simulations over the second half of the 20th century. Our results show that the reanalysis-estimated HPR is largest over Intertropical Convergence Zone (ITCZ) regions, with seasonal mean values of -0.22 W m^{-2} (-2.31 to 0.29 W m^{-2}) in DJF and -0.28 W m^{-2} (-2.89 to 0.24 W m^{-2}) in JJA. These values are consistent with the model-simulated HPR patterns. In DJF, the HPR leads to a weaker equator-pole surface heating difference and therefore, weakens northern stationary waves. The consequent changes of the heat and moisture advection result in noticeable TLSA warming effects (for example, $+0.53 \text{ K}$ over northern Eurasia and $+0.46 \text{ K}$ over central North America) and cooling effects (for example, -0.62 K over Alaska and -0.42 K over central Asia) at regional scales. These temperature changes help to reduce the TLSA biases in the model. In JJA, the TLSA changes slightly because of the weak stationary wave responses during the northern summer.

1. Introduction

In climate models, the land surface energy balance should be expressed as:

$$C \frac{\partial T}{\partial t} = R_{net} - \lambda E - H - F + H_{pr} \quad (1)$$

where T is the surface temperature, R_{net} is the net radiation, λE and H are the turbulent fluxes of latent and sensible heat, F is the heat flux into the subsurface, and H_{pr} is the precipitation-induced sensible heat flux (HPR). However, HPR is always neglected in models because it has a relatively small magnitude in long-term climatological simulations [Curry *et al.*, 1999].

HPR is generated and transferred between the land surface and rainwater with a different temperature. This transfer can be large during heavy rainfall events and can significantly affect the short-term land surface energy budget. For example, in midlatitude and low latitude, the cooling effect of HPR on the land surface can be used to explain why we feel much cooler during heavy summer rainfall events. However, when HPR is averaged over longer timescales, the magnitude becomes much smaller. Kollet *et al.* [2009] calculated the HPR of the Haarweg Meteorological Station in Wageningen, Netherlands, with a land surface model and found that the HPR was as large as -60 W m^{-2} during the rainfall events in 2002. This large value led to a topsoil temperature decrease of $> 1 \text{ K}$ within 1 day after the heavy rainfall stopped. However, the mean HPR over the entire year was only -1.5 W m^{-2} . Gosnell *et al.* [1995] found that the HPR could reach -200 W m^{-2} during an intense rain event in the Tropic Ocean-Global Atmosphere Coupled Ocean-Atmosphere Response Experiment (TOGA-COARE). This value sharply cooled the local surface sea temperature in the short-term. But when averaged over the entire period, the HPR was approximately -2.5 W m^{-2} only. Anderson *et al.* [1998] found that the HPR in the Western Pacific Warm Pool was an important contributor to the net surface heating when it was raining, with the value ranging from -65.0 to -204 W m^{-2} . Hence, the HPR accounted for

15–60% of the net heat flux during a single rainfall event. However, the mean HPR value over a 4 month observational period was only -2.8 W m^{-2} .

These studies indicate that HPR could have a notable effect on the local surface air temperature during a heavy rainfall event, particularly in the tropics where the cooling effect is dominant due to the abundant rainfall and generally negative temperature differences between the land surface and rainwater. However, the effect of HPR on time scales of months or longer remains unclear. For oceans, a preliminary analysis by *Flament and Sawyer* [1995] suggested that the mean HPR value in the Intertropical Convergence Zone (ITCZ), where the annual rainfall reached 3000 mm, was approximately -7 W m^{-2} . This value accounted for 23% of the maximum net heat flux and, if ignored, it would produce erroneous heating of 1 K per year in the mixed oceanic layer. *Anderson et al.* [1998] also mentioned that in the western tropical Pacific, the mean HPR of -2.8 W m^{-2} during a 4 month observational period (when the mean precipitation rate was 10.3 mm day^{-1} and the assumptive mean rainwater-sea surface temperature difference was -5 K) was 15% of the net surface heat flux. In addition, if the HPR was included, the surface buoyancy flux was also reduced by 6.5%. Therefore, the HPR in the tropical ocean should be included to fully close the surface energy balance and to quantify the buoyancy forcing, even though the HPR was the overall smallest term in the surface energy budget. For land, the long-term climate effects of HPR have not been comprehensively studied.

An accurate simulation of the land surface air temperature (TLSA) requires climate models to correctly represent land-atmosphere interactions in every component of the coupled model [*Lawrence et al.*, 2012]. HPR tends to affect the components of the land surface energy balance system and to change the energy budget in canopy and soil processes. *Kollet et al.* [2009] noted that the HPR in a single heavy rainfall event could influence the ground heat flux for a period of up to 1 month, and the cumulative influence of multiple rainfall events may be notable. *Boike et al.* [2003] and *Gillett and Cullen* [2011] also concluded that the HPR could play an important part in glacier ablation and snow cover melt by changing their albedos and modifying the absorption of the shortwave solar radiation at the surface. All these studies motivated us to include HPR into land surface models to improve TLSA simulations.

The Community Earth System Model 1 (CESM1) can generally capture the observed large-scale spatial and temporal patterns of TLSA, with the biases reduced and the annual cycle improved in many locations, particularly over high latitudes when CESM1 is compared to its previous versions as the Community Climate System Model (CCSM) [*Lawrence et al.*, 2012]. However, CESM1 (with atmospheric CAM4 physics) still has positive, annual mean TLSA biases over the Canadian Shield, Central U. S., Central Eurasia, and Siberia, with particularly warm summer biases over Central Canada and Eurasia [*Gent et al.*, 2011; *Lawrence et al.*, 2012; *Subin et al.*, 2012]. The largest annual mean TLSA biases of 2–4 K in CESM1 are located over Europe and western Asia, which may partially be attributed to deficiencies in simulating frozen soil hydrology and energy processes [*Lawrence et al.*, 2012; *Subin et al.*, 2012]. Because the HPR can change the land surface energy budget and surface properties, the inclusion of HPR in CESM1 may help to correct some of the particular TLSA biases.

In this study, we first estimate HPR on a global scale using satellite and reanalysis data sets. And then, we use CESM1 (with atmospheric CAM4 physics and the prescribed sea surface temperature) to investigate whether the inclusion of HPR in the model can help to reduce TLSA biases. In the model experiments, the HPR is calculated in CLM4 (the land component of CESM1) and is introduced into the land surface energy balance system to analyze the HPR effects. The model simulations over the entire second half of the 20th century are used to evaluate HPR contributions to the simulated TLSA accuracy.

2. Data and Methodology

2.1. Parameterization of Precipitation-Induced Sensible Heat Flux

The sensible heat flux (W m^{-2}) induced by precipitation (HPR) can be expressed as:

$$H_{pr} = C_{pr} \rho (T_{pr} - T_s) r \quad (2)$$

where C_{pr} is the specific heat capacity of rain or snow, ρ is the density of the precipitation, r (mm s^{-1}) is the rate of the precipitation, and T_s and T_{pr} are the land surface temperature and the precipitation-water temperature, respectively. A negative H_{pr} value signifies a loss of heat from the land surface to the rainwater.

In equation (2), T_{pr} must be parameterized due to the lack of rainwater temperature observations. According to previous studies [*Byers et al.*, 1949; *Kinzer and Gunn*, 1951; *Kincaid and Longley*, 1989; *Flament and*

Sawyer, 1995; Gosnell et al., 1995; Anderson et al., 1998], falling raindrops/snowflakes can reach an equilibrium temperature that is near the ambient wet-bulb temperature. Therefore, T_{pr} is taken as the atmospheric wet-bulb temperature just above the Earth's surface. The details for calculating the wet-bulb temperature are given by Anderson et al. [1998].

2.2. Parameterization of the Land Surface Energy Balance

The HPR is incorporated into two physical processes as follows:

1. Canopy energy balance: Assuming that the specific heat capacity of the canopy is 0, the canopy energy conservation in CLM4 is expressed as $R_{net,v} - H_v - \lambda E_v = 0$. This energy balance equation is updated by including HPR as:

$$R_{net,v} - H_v - \lambda E_v + H_{pr} = 0 \quad (3)$$

Note that the HPR, which is expressed here as $H_{pr} = C_{pr} \rho (T_{pr} - T_v) q_{int,r}$, is computed with the precipitation rate intercepted by canopy leaves $q_{int,r}$ (mm s^{-1}). T_v is the canopy leaf temperature, and $R_{net,v}$ is the net radiation absorbed by the canopy.

2. Ground surface energy balance: The ground surface temperature (T_g) is considered as the temperature at the top layer of the ground in CLM4 and is solved through the equation $C_g \Delta z_g \frac{\partial T_g}{\partial t} = R_{net,g} - H_g - \lambda E_g + F$, where C_g and Δz_g are the volumetric snow/soil heat capacity and the thickness of the top ground layer, and F is the snow/soil heat flux from the underlying layer to the top layer. The modified ground surface energy conservation induced by HPR is given as:

$$C_g \Delta z_g \frac{\partial T_g}{\partial t} = R_{net,g} - H_g - \lambda E_g + H_{pr} + F \quad (4)$$

In this study, two different situations are considered when calculating HPR. For bare ground, the HPR is calculated with equation (2); for vegetated surfaces, the precipitation is divided into the throughfall, which falls directly onto the snow/soil surface with the rain temperature T_{pr} , and the canopy drip, which drips off the vegetation with the canopy temperature T_v . Hence, the HPR into the ground is expressed as:

$$H_{pr} = C_{pr} \rho (T_{pr} - T_g) q_{thru} + C_{pr} \rho (T_v - T_g) q_{drip} \quad (5)$$

where q_{thru} (mm s^{-1}) and q_{drip} (mm s^{-1}) are the rates of throughfall and canopy drip, respectively. The HPR is also considered for calculating the energy excess or deficit when a phase change of the land surface water occurs. Detailed simulation schemes of the canopy/ground energy conservation are provided by Oleson et al. [2010].

2.3. Data Sets

2.3.1. Satellite and Reanalysis Data for Estimating HPR

In order to take into account the global distribution and magnitude of HPR, we first calculate HPR using satellite and reanalysis data sets. We use the CPC Merged Analysis of Precipitation (CMAP) monthly averaged data for the precipitation rate (r). This product is obtained by combining the gauge data and five satellite estimates, with gaps filled by NCEP/NCAR precipitation values [Xie and Arkin, 1997]. It is globally on a 2.5° by 2.5° grid. The rainwater temperature (T_{pr}) is approximated by the wet-bulb temperature, and the data on the land-surface air temperature, specific humidity, and pressure (which are required for calculating the wet-bulb temperature) are derived from the European Centre for Medium-Range Weather Forecasts (ECMWF) Interim Reanalysis data set. The land surface temperature (T_s) is also derived from the skin temperature of the ECMWF Interim Reanalysis. These reanalysis data sets, which have a resolution of 1.25° by 1.25° , are reprojected to the lower resolution of CMAP data. Using equation (2), we obtain the monthly mean values of HPR on 2.5° by 2.5° latitude-longitude grids over a 27-year period from 1979 to 2005.

2.3.2. Data for a Comparison With the Simulated Results

To compare to the simulated TLSA with CESM1, we use the Willmott and Matsuura (WM) data (V 1.02) as observational records. The WM data provide a monthly averaged detailed land surface air temperature spanning 1950–1999 [Willmott and Matsuura, 2001]. This product is available on a 0.5° by 0.5° grid and is reprojected to the default 1.9° by 2.5° CLM4 resolution.

2.4. Climate Model Experiments

In our simulations, the control runs without HPR (CNTL) are performed for the entire historical period from 1850 to 2005 and are forced by the prescribed sea ice and sea surface temperature (SST) from the global

HadISST OI data set (prior to 1981) and the Smith/Reynolds EOF data set (after 1981). The natural forcings (e.g., volcanoes and solar irradiance) and anthropogenic emissions (e.g., CO₂ and aerosols) from the historical data sets also drive the CNTL simulations. The perturbation runs (MHPR) are performed with the same forcings as CNTL, with the addition of the new land surface energy budget scheme. The HPR in the new scheme is estimated in CLM4 with the approximated T_{pr} (the atmospheric wet-bulb temperature) calculated from the transferred atmospheric air temperature, specific humidity, and pressure from the atmospheric model CAM4. We perform five 156-year control runs and five 156-year perturbation runs with different initial conditions derived from the first control integration. Unless otherwise noted, the following discussions focus on the ensemble mean differences between the control and perturbation simulations, rather than the individual runs, because averaging over multiple members helps to enhance the forcing signal related to HPR and reduces the noise from the internal variability and errors in the individual simulations [Zhou *et al.*, 2009]. To maintain the temporal consistency with the WM data, we primarily examine the seasonal means of the model outputs over the second half of the 20th century (1950–1999). Therefore, the first 100 years of simulations from 1850 in each run are discarded, which is sufficient for the spinup of climate models. All of the simulations are run at a 1.9° by 2.5° resolution. Because the SST is specified, the present research addresses the response of TLSA to HPR over land only. Fully coupled simulations are a goal for future studies.

3. Results

3.1. HPR Estimated by Satellite and Reanalysis Data and Simulated by CESM

Figures 1a and 1c display the seasonally averaged latitude-longitude plots of the HPR calculated from the satellite and reanalysis data. The geographical distribution of the HPR is closely tied to the distribution of the precipitation and the land surface temperature, with a large HPR over ITCZ regions. During the northern winter (DJF), the HPR average is -0.22 W m^{-2} , with notable values up to -2.31 W m^{-2} over the Subtropical Convergence Zone in northern Australia, central South America, and southern Africa. Meanwhile, positive values of HPR, up to 0.29 W m^{-2} , appear over central and northern Asia, Europe, western North America, and Greenland because the rainwater temperature is generally higher than the winter-time land surface temperature over northern extratropical regions, and thus, the land receives additional heat from the precipitation at these locations. During the northern summer (JJA), the mean HPR is -0.28 W m^{-2} , with a wider range from -2.89 to 0.24 W m^{-2} . Large values of HPR primarily appear over North America, the southern Sahel regions, the Indian subcontinent, and Eurasia. In these regions, the mean surface precipitation rate is nearly 2.5 mm day^{-1} , and the mean rainwater-land surface temperature difference is approximately -13°C . Hence, the mean HPR value reaches nearly -1.6 W m^{-2} , which is close to the HPR calculated by Kollet *et al.* [2009] at the Haarweg Meteorostation.

In the CLM4 model simulations (Figures 1b and 1d), the seasonally averaged HPR has almost the same pattern as the satellite and reanalysis estimations, particularly in the midlatitude and low latitude where the HPR is concentrated. The total mean HPR added to the canopy and ground energy balance system is -0.31 W m^{-2} (up to -2.89 W m^{-2}) in DJF and -0.34 W m^{-2} (up to -2.0 W m^{-2}) in JJA. The slight difference in the HPR magnitudes between the reanalysis estimation and the model simulation could be attributed to the model biases for the precipitation rate and the simulated rainwater-land surface temperature difference. The overall consistent HPR patterns indicate that the quantity of the simulated HPR, which is added to the land surface processes, is reasonable. We have compared the seasonal mean values of the HPR over the first 20 years and the last 20 years of the 20th century and found few differences. Therefore, the simulated HPR can be considered annually time-invariant and can reflect the primary HPR climatology over the 20th century.

In both the reanalysis estimation and the model simulation, the large negative HPR is primarily concentrated in low latitudes and becomes smaller or even turns positive in high latitudes. This latitudinal structure is important for explaining the atmospheric responses to HPR as discussed later.

3.2. Effects of HPR on CESM1 Simulations for TLSA

Because the global annual mean HPR added to the land surface energy budget is only -0.27 W m^{-2} and the SST is prescribed, the simulated global mean TLSA responses are insignificant for both the annual mean (approximately -0.02 K) and the seasonal mean (for example, the DJF mean is -0.01 K and the JJA mean is

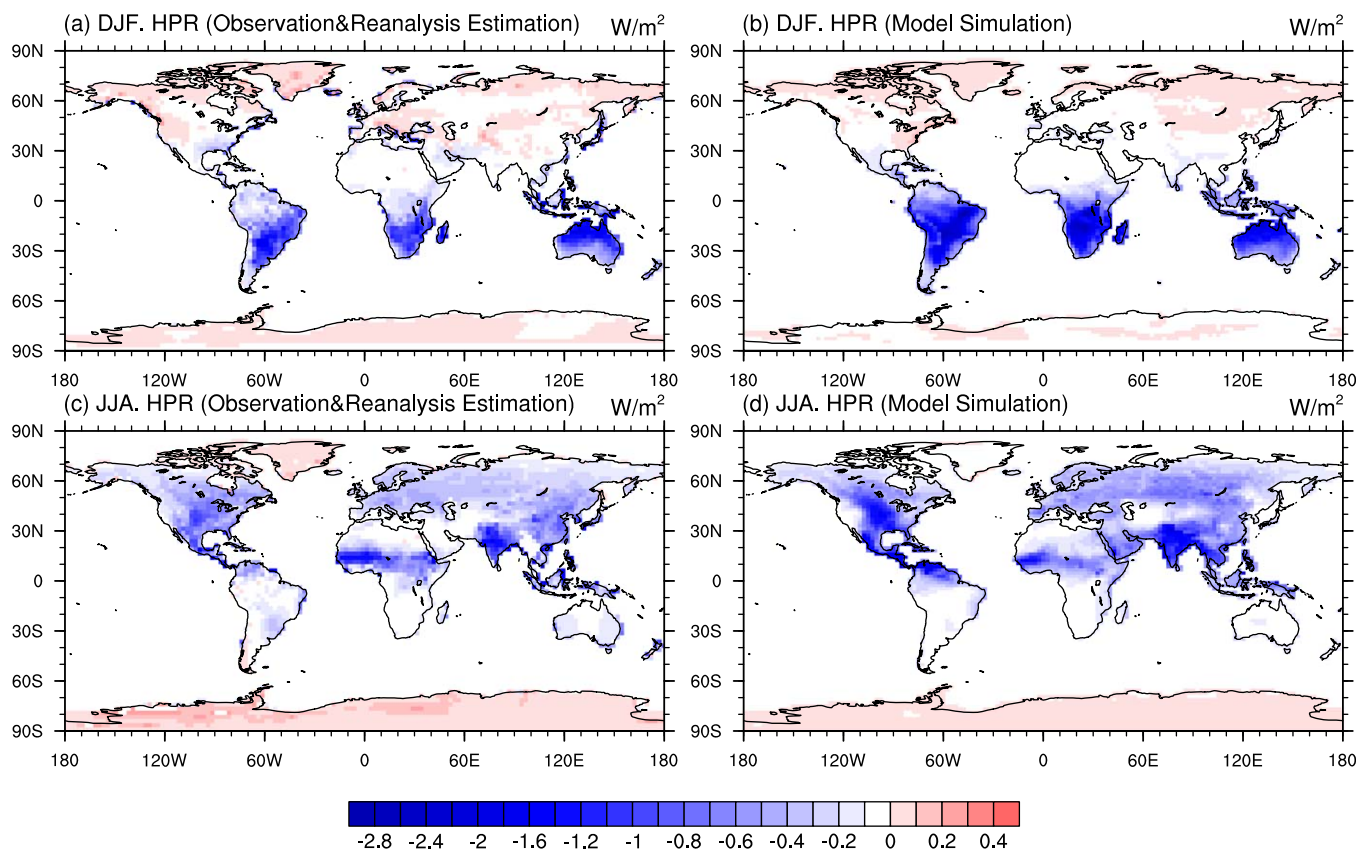


Figure 1. Geographical distribution of the DJF and JJA precipitation-induced sensible heat flux (HPR) calculated with the CMAP and ECMWF Interim Reanalysis data (top) and the CLM4 model (bottom) averaged for the period of 1979–2005. The ocean data are marked out.

–0.02 K). However, the HPR induces noticeable regional effects on the TLSA simulations, with an overall reduction of the TLSA biases compared with the observed WM data, particularly in northern high latitudes during the winter.

The TLSA biases in DJF in the CLM4 control simulation are shown in Figure 2a. Similarly to the AMIP simulations in many other models [Gates *et al.*, 1999], the large TLSA biases in high latitudes can reach over 10 degrees. Several major features are noticeable in the northern extratropics, such as a warm bias in Alaska and a cold bias in the remainder of North America, warm biases in Greenland, the Mediterranean and central Asia, and cold biases in northern Eurasia and China. Figure 2b shows the differences of the simulated TLSA induced by HPR, which have signs opposite to the TLSA biases in the control simulation. The cooling effects in Alaska, Greenland, and central Asia reduce the warm biases by up to –0.94 K, while the warming effects in central North America, northern Eurasia, northern China, and Mongolia reduce the cold biases by as much as 1.07 K. Therefore, the HPR exerts statistically significant regional effects on the TLSA simulations. Although the cooling effect over Sahel regions and the warming effect over central Siberia may slightly exacerbate the TLSA biases, the spatial correlation between the TLSA biases (Figure 2a) and the TLSA changes induced by HPR (Figure 2b) is –0.3, implying that the HPR overall helps to reduce the TLSA biases in the right direction at the global scale. A comparison of Figure 2 with Figure 1 clearly shows that the HPR-induced temperature changes do not spatially correlate with the HPR in a direct manner. Therefore, indirect effects of the HPR may play a major role in the temperature responses during DJF, which will be discussed later.

In JJA, the control simulation shows large warm biases of TLSA in midlatitude and high latitude in the northern extratropics and cold biases in low latitudes from 30°N to 30°S (Figure 2c). Similar biases have been revealed in coupled ocean-atmosphere models [Gent *et al.*, 2011]. However, the TLSA does not noticeably respond to the HPR, except for a significant but regional cooling effect near the northern Ural Mountains (Figure 2d). The TLSA biases are reduced but with a much smaller magnitude than those in DJF. Therefore, the HPR may have a negligible effect on the TLSA simulation in JJA.

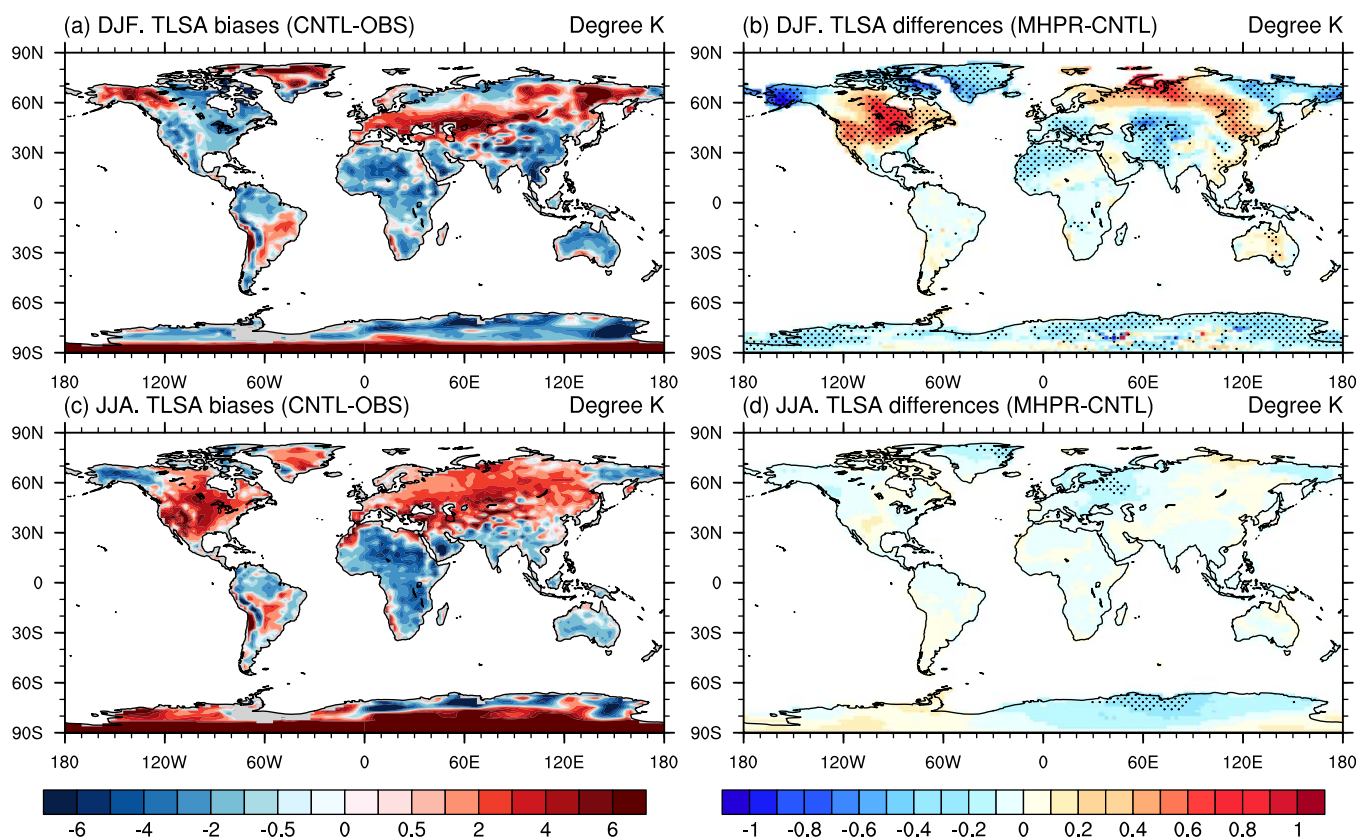


Figure 2. Geographical distribution of the land surface air temperature (TLSA) biases in the standard model compared with the observed Willmott and Matsuura data (left) and the simulated TLSA differences (the perturbation runs minus the control runs) induced by the precipitation-induced sensible heat flux (HPR) (right) in DJF and JJA. The areas exceeding the 95% t-test confidence level are stippled. All of the values are averaged for the period of 1950–1999. The ocean data are marked out.

4. Discussions

The ensemble mean TLSA changes show that the HPR induces only slight TLSA responses in JJA, but it has a strong impact on the TLSA simulations in DJF. We also assessed the spatial distribution of the TLSA responses in each ensemble run and found a similar TLSA change pattern (supporting information S1), indicating that our results are robust. In DJF, the TLSA changes are generally correlated with the HPR-induced changes of the net ground heat flux (supporting information S2). Because the regions with the significant TLSA and ground heat flux changes are not spatially coupled with the HPR sources, the simulated temperature responses must be related to the horizontal transportation of the heat or water mass carried by the modified large-scale wind. Therefore, the TLSA responses, along with the land surface energy redistribution, are more likely caused by changes in the dynamical atmospheric circulation, which could induce remote climatological responses on long timescales.

As shown in Figure 1, the direct forcing of the HPR in DJF has a surface cooling effect in ITCZ regions and a slight warming effect in northern midlatitude and high latitude. This latitudinal distribution of HPR may reduce the equator-pole difference of the heat input to the land surface, and thus change the stationary wave activities in the Northern Hemisphere [Subin *et al.*, 2012]. As a result, the changes in wind fields, along with the altered horizontal heat and moisture advection, may lead to the TLSA changes.

To test this hypothesis, we examine the changes in the stationary waves at the Earth’s surface, which can be identified by the sea level pressure field (PSL) [Nigam and Deweaver, 2003]. Generally, the PSL can be broadly characterized as high pressure over continents and low pressure over comparatively warmer northern oceans during DJF (Figure 3a). Figure 3b shows the PSL responses to the HPR and reveals that the HPR induces surface pressure changes with positive values over the northern Atlantic (Iceland Low) and the northern Pacific (Aleutian Low) and with negative values over western North America and central Asia. The

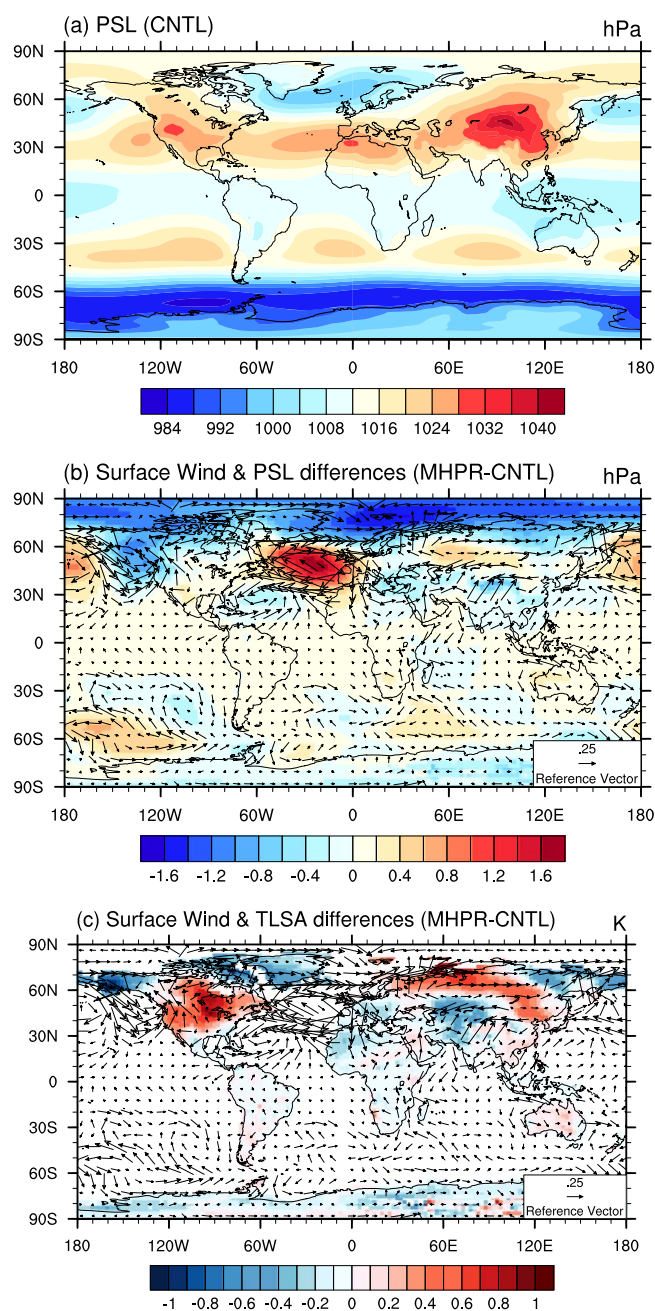


Figure 3. Geographical distribution of the sea level pressure field (PSL) in the control simulation (a), the simulated PSL changes overlaid by the surface wind anomalies (b) and the simulated TLSA differences overlaid by the surface wind anomalies (c) in DJF. All of the values are averaged for the period of 1950–1999.

(Figure 4b). Although the anomalous high pressure over the Atlantic may enhance the ridge in the eastern Atlantic, the weakened trough in the western Atlantic, the anomalous low pressure over central Asia and the anomalous high pressure over central North America and northern Eurasia are all in the opposite phase to the original 500 hPa geopotential height patterns, indicating that the amplitude of stationary wave is weakened. As a result, the wind anomalies change the moisture advection by increasing the moisture flux over central North America and north Eurasia where more moisture content is transported from the northern Pacific and northern Atlantic (Figure 4c). The subsequent increase of the water vapor and the total cloud cover in these regions leads to the enhanced downward longwave radiation (Figures 4d–4f), which creates

resulting reduction in the high-low pressure difference compared to the original PSL pattern reflects a weakening of the intensity of the stationary wave. Consequently, the surface wind anomalies would alter the surface latitudinal heat advection and cause the TLSA changes. For example, the anomalous trough over western North America produces southerly wind anomalies over North America (Figure 3c), which helps to advect less cold air from high latitudes compared to the regular surface wind over North America, thus resulting in a center of warm TLSA differences there (~ 0.46 K). Similarly, the trough-induced northwesterly wind anomalies over Alaska lead to the cooling TLSA responses (~ -0.62 K). It is also seen from Figure 3c that the negative TLSA changes over Greenland (~ -0.39 K) result from the cold-air advection by the anomalous northwesterly flow, while the positive TLSA changes over northern Eurasia (~ 0.53 K) and northern China and Mongolia (~ 0.22 K) are produced by the warm-air advection by the southwesterly wind anomalies.

The weakening of stationary waves can also be seen in the 500 hPa geopotential height (Geo). In the northern hemisphere winter, the stationary waves are characterized by large-scale ridges in the eastern Atlantic and eastern Pacific and troughs in the western Atlantic and western Pacific (Figure 4a). The HPR induces the opposite phase of the 500 hPa geopotential height changes with an anomalous trough in the eastern Pacific and an anomalous ridge in the western Pacific

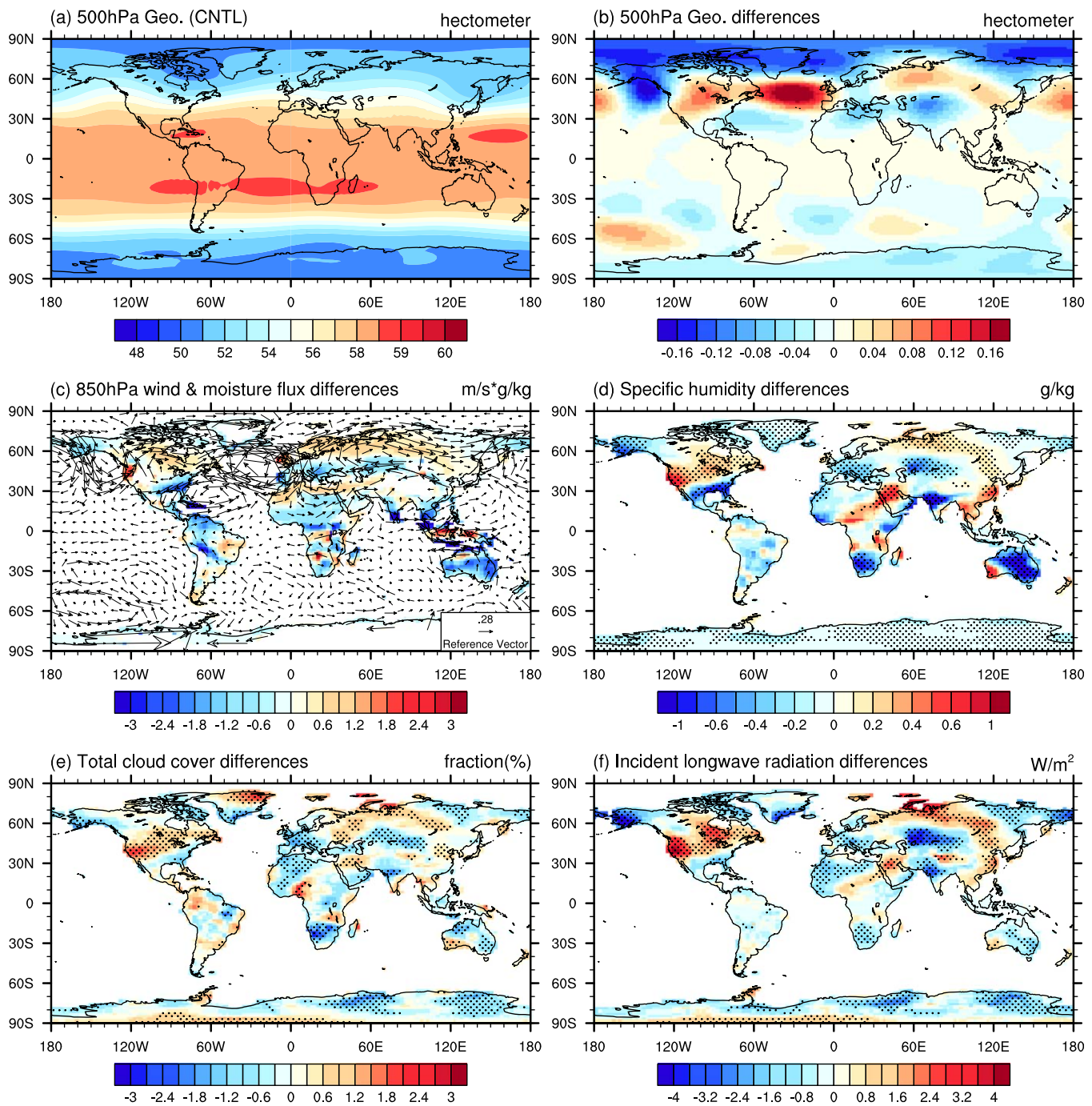


Figure 4. Geographical distribution of the 500 hPa geopotential height field (500 hPa Geo) in the control simulation (a), the simulated 500 hPa Geo changes (b), the simulated 850 hPa moisture flux changes overlaid by the 850 hPa wind anomalies (c), the simulated atmospheric specific humidity changes (d), the simulated total cloud cover changes (e), and the simulated downward longwave radiation changes (f) in DJF. The areas exceeding the 95% t-test confidence level are stippled. All of the values are averaged for the period of 1950–1999.

positive changes of TLSA [Zhou *et al.*, 2009]. Similarly, the decreased moisture flux over central Asia leads to the reduced water vapor and cloud cover, which decrease the downward longwave radiation at the surface and thus result in the central Asian cooling.

We therefore propose a possible hypothesis to explain the HPR effect on winter TLSA responses. In DJF, the direct forcing of the HPR leads to a weaker equator–pole gradient of surface heating, which in turn weakens the stationary waves in the simulations as shown by the changes of the PSL and 500 hPa geopotential

height. The resulting anomalous wind changes the heat and moisture advection, and thus changes atmospheric water vapor and cloud cover. As a result, the modified downward longwave radiation forcing at the surface changes the TLSA responses to the HPR. In JJA, the latitudinal distribution of the HPR in the northern hemisphere is relatively uniform, and hence hardly changes the equator-pole heating gradient. In addition, the stationary wave activities are weakest in the northern summer [Nigam and Deweaver, 2003]. Therefore, the HPR has no noticeable effects on the TLSA simulations in JJA.

Despite the small magnitude of HPR at the global scale, the TLSA changes induced by HPR at regional scales are comparable to those induced by deforestations (up to 2 K) and the anthropogenic heating resulting from the energy consumption (up to 1 K of warming in the northern winter) [Zhang *et al.*, 2013]. In the context of global warming, the impact of HPR is expected to increase with the projected increase of heavy precipitation events and changes in the latitudinal precipitation distribution. However, our hypothesis is based on the simulations from one model. Further studies are required to examine the effects of HPR using multiple models to identify more accurate and robust climatological responses to HPR. The HPR effects on the global (land and ocean) climatology will be also explored in the future with fully coupled models.

5. Conclusions

In this study, we use satellite and reanalysis data sets to estimate HPR on a global scale and use CESM1 (with CAM4 physics and the prescribed sea surface temperature) to investigate the effect of HPR on TLSA simulations. The satellite and reanalysis estimations showed that the HPR has the largest value over ITCZ regions. The mean HPR is -0.22 W m^{-2} (-2.31 to 0.29 W m^{-2}) in DJF and -0.28 W m^{-2} (-2.89 to 0.24 W m^{-2}) in JJA. The model-simulated HPR has nearly the same pattern as the satellite and reanalysis estimations in midlatitude and low latitude. The magnitude of regional impacts of HPR on TLSA patterns is comparable to that of other factors, such as changes in O_3 and aerosol concentrations and land use, which are described in the most recent IPCC assessment released in 2013.

The HPR shows only slight impacts on the global mean TLSA, but it has significant regional cooling or warming effects over midlatitude and high latitude in the northern winter. These effects help to reduce the TLSA biases in the standard model. In DJF, the TLSA is indirectly affected by HPR via changes of the atmospheric circulations, which are caused by a weak surface energy input gradient between the equator and poles that reduces the stationary wave amplitudes. Hence, the noticeable warming effect (for example, 0.46 K and 0.53 K averaged over North America and North Eurasia, respectively) and cooling effect (for example, -0.62 K , -0.39 K and -0.42 K averaged over Alaska, Greenland and central Asia, respectively) are likely driven by the anomalous heat and moisture advection carried by the wind anomalies. Although the TLSA simulations are only slightly affected in JJA, the substantially reduced seasonal TLSA biases by up to 1 K in DJF indicate that it is beneficial to include the HPR in the land-surface energy budget in current climate models.

References

- Anderson, S. P., A. Hinton, and R. A. Weller (1998), Moored observations of precipitation temperature, *J. Atmos. Oceanic Technol.*, *15*, 979–986, doi:10.1175/1520-0426(1998)015<0979:MOOPT>2.0.CO;2.
- Boike, J., K. Roth, and O. Ippisch (2003), Seasonal snow cover on frozen ground: Energy balance calculations of a permafrost site near Ny-Alesund, Spitsbergen, *J. Geophys. Res.*, *108* (D2), 8163, doi:10.1029/2001JD000939.
- Byers, H. R., H. Moses, and P. J. Harney (1949), Measurement of rain temperature, *J. Meteorol.*, *6*, 51–55, doi:10.1175/1520-0469(1949)006<0051:MORT>2.0.CO;2.
- Curry, J. A., C. A. Clayson, W. B. Rossow, R. Reeder, Y. C. Zhang, P. J. Webster, G. Liu, and R. S. Sheu (1999), High-resolution satellite-derived dataset of the surface fluxes of heat, freshwater, and momentum for the TOGA COARE IOP, *Bull. Am. Meteorol. Soc.*, *80*, 2059–2080, doi:10.1175/1520-0477(1999)080<2059:HRSDDO>2.0.CO;2.
- Flament, P., and M. Sawyer (1995), Observation of the effect of rain temperature on the surface heat flux in the intertropical convergence zone, *J. Phys. Oceanogr.*, *25*, 413–419, doi:10.1175/1520-0485(1995)025<0413:OOTEOR>2.0.CO;2.
- Gates, W. L., et al. (1999), An overview of the results of the atmospheric model intercomparison project (AMIP I), *Bull. Am. Meteorol. Soc.*, *80*, 29–55, doi:10.1175/1520-0477(1999)080<0029:AOTRO>2.0.CO;2.
- Gent, P. R., et al. (2011), The community climate system model version 4, *J. Clim.*, *24*, 4973–4991, doi:10.1175/2011JCLI4083.1.
- Gillett, S., and N. J. Cullen (2011), Atmospheric controls on summer ablation over Brewster Glacier, New Zealand, *Int. J. Climatol.*, *31*(13), 2033–2048, doi:10.1002/joc.2216.
- Gosnell, R., C. W. Fairall, and P. J. Webster (1995), The sensible heat of rainfall in the tropical ocean, *J. Geophys. Res.*, *100*(C9), 18,437–18,442, doi:10.1029/95JC01833.
- Kincaid, D. C., and T. S. Longley (1989), A water droplet evaporation and temperature model, *Trans. ASAE*, *32*, 457–463.

Acknowledgments

We are grateful to National Center for Atmospheric Research (NCAR) for providing the source code of CESM model. NCAR is sponsored by the National Science Foundation. Also thanks to the NOAA/OAR/ESRL PSD, Boulder, Colorado, USA for providing CMAP Precipitation data (<http://www.esrl.noaa.gov/psd/>), Kenji Matsuura and Cort J. Willmott (with support from IGES and NASA) for providing terrestrial air temperature records (http://climate.geog.udel.edu/~climate/html_pages/download.html#ghcn_T_P2), and European Centre for Medium-Range Weather Forecasts for providing ECMWF Interim data sets. This study was supported by the program of the Intellectual Introduction Project for the Discipline Innovation in China University System (111 Program), the Natural Science Foundation of China (under Grants 40875062 and 40225013), the R&D Special Fund for Nonprofit Industry (Meteorology, GYHY201206013 and GYHY200706025), and the Fundamental Research Funds for the Central Universities (2013YB36). We thank the editors and two anonymous reviewers for their thorough and constructive review, and thank Robert E. Dickinson, Aiguo Dai, and Guoyue Niu for their helpful discussions.

- Kinzer, G. D., and R. Gunn (1951), The evaporation, temperature, and thermal relaxation-time of freely falling water drops, *J. Meteorol.*, *8*, 71–83, doi:10.1175/1520-0469(1951)008<0071:TETATR>2.0.CO;2.
- Kollet, S. J., I. Cvijanovic, D. Schuettemeyer, R. M. Maxwell, A. F. Moene, and P. Bayer (2009), The influence of rain sensible heat and subsurface energy transport on the energy balance at the land surface, *Vadose Zone J.*, *8*(4), 846–857. doi:10.2136/vzj2009.0005.
- Lawrence, D. M., K. W. Oleson, M. G. Flanner, C. G. Fletcher, P. J. Lawrence, S. Levis, S. C. Swenson, and G. B. Bonan (2012), The CCSM4 land simulation, 1850–2005: Assessment of surface climate and new capabilities. *J. Clim.*, *25*, 2240–2260, doi:10.1175/JCLI-D-11-00103.1.
- Nigam, S., and E. Deweaver (2003), Stationary waves(oroographic and thermally forced), in *Encyclopedia of Atmospheric Sciences*, edited by J. Holton, J. Pyle and J. Curry, pp. 2121–2137, Oxford Academic Press, London, U. K.
- Oleson, K. W., D. M. Lawrence, G. B. Bonan, M. G. Flanner, E. Kluzek, P. J. Lawrence, S. Levis, S. C. Swenson, and P. E. Thornton (2010), *Technical Description of version 4.0 of the Community Land Model (CLM)*. NCAR Tech. Note, NCAR/TN-478 +STR, 77–113.
- Subin, Z. M., L. N. Murphy, F. Li, C. Bonfils, and W. J. Riley (2012), Boreal lakes moderate seasonal and diurnal temperature variation and perturb atmospheric circulation: Analyses in the Community Earth System Model 1 (CESM1). *Tellus Ser. A*, *64*, 15639, doi:10.3402/tellusa.v64i0.15639.
- Willmott, C. J., and K. Matsuura (2001), *Terrestrial Air Temperature and Precipitation: Monthly and Annual Time Series (1950–1999) (Version 1.02)*. [Available at http://climate.geog.udel.edu/~climate/html_pages/download.html.]
- Xie, P., and P.A. Arkin (1997), Global precipitation: A 17-year monthly analysis based on gauge observations, satellite estimates, and numerical model outputs, *Bull. Am. Meteorol. Soc.*, *78*, 2539–2558.
- Zhang, G. J., M. Cai, and A. Hu (2013), Energy consumption and the unexplained winter warming over northern Asia and North America, *Nat. Clim. Change*, *3*, 466–470, doi:10.1038/nclimate1803.
- Zhou, L., R. E. Dickinson, A. Dai, and P. Dirmeyer (2009), Detection and attribution of anthropogenic forcing to diurnal temperature range changes from 1950 to 1999: Comparing multi-model simulations with observations, *Clim. Dyn.*, *35*, 1289–1307, doi: 10.1007/s00382-009-0644-2.